21

Measuring and Visualizing EOD Fields

Brian Rasnow

U4EA Enterprises Inc., 1000 S. Ventu Park Rd., Newbury Park, CA 91320. e-mail: rasnow@alumni.caltech.edu

ABSTRACT

Understanding the biophysics of electroreception by weakly electric fish is likely to require measuring, visualizing, and modeling the fish's electric organ discharge (EOD) and its perturbations from objects and other fish. This chapter describes the theory and methods for detecting, filtering, transforming, and visualizing the spatiotemporally complex EOD field.

Key Words: Electronics; Signal processing; Mapping

1. INTRODUCTION

The electrosensory world of weakly electric fish is foreign to our intuitions, since the physics of electric sense is fundamentally different from any innate sensory modality. Electric sense differs from sight, hearing, touch, taste, and smell in comparable ways that those senses differ from each other. Our efforts to understand electric sense are, therefore, analogous to a blind person exploring vision or a deaf individual trying to perceive sound. Try to imagine being blind and using a CCD camera to capture visual data, transforming the data with a computer, and transducing the results with relays and speakers into tactile and auditory representations that can be directly perceived. Invariably, the richness and qualia (Dennett, 1988) of the visual experience will be different. On the other hand, the emotional richness and qualia we experience with our innate senses seems to offer little, and perhaps even confounds our attempts to understand the underlying biophysics of our

sensory perceptions. Thus, we approach electric sense without intuition to guide, or falsely bias our understanding.

This chapter describes some methods and technologies to blindly explore the electrosensory world. Electrodes, amplifiers, analog-to-digital converters (ADCs), Fourier transforms, Delaunay tessalations are some of the analogs to photodetectors, walking sticks, and headphones (Fig. 21.1). These advanced gadgets were used to measure and map the fish's self-generated electric potential, compute its gradient (the electric field vector), render the field maps as animated pseudocolor images, construct analytical models and simulations, and study the properties of electrosensory images. This exercise revealed new glimpses of a complex electric sensory world rich in spatiotemporal structure. The careful measurements, analysis, and visualization, in turn, permitted the construction of an intuitive foundation that has supported new hypotheses about the biophysics and neurocomputational algorithms underlying electric perception, and suggested further directed experiments and explorations of the electrosensory world (Rasnow and Bower, 1997; Assad et al., 1999).

Electrosensory systems have evolved exquisite sensitivity to weak perturbations of their electric organ discharge (EOD) caused by either local objects with different conductivity or dielectric constant than the water, and/or from superposition of electric discharges from other electric fish. The corresponding electromotor system (the electric organ and its neural control circuits) have co-evolved incredible stability, not only in the fundamental frequency of discharge, but also in the spatial and temporal details of the waveform. Behavioral and mapping studies suggest that *Apteronotus* can detect objects that perturb its millivolt EOD by 0.01%. Eavesdropping on such perturbation signals with accuracy and precision is challenging (if not impossible) without inducing artifacts of comparable or greater magnitude. It requires great care and consideration of numerous factors including: temperature; anesthesia; oxygen; electrical effects of the tank walls, electrodes, and nearby structures; electronics; and signal-processing algorithms.

The following sections will elaborate methods for measuring EODs and EOD perturbations and processing and visualizing the resulting voluminous data. A mixture of methods, theory, and tips will hopefully provide the reader with adequate knowledge and confidence to undertake field mapping as a source or test of their hypotheses.

2. RECORDING TANK

A large recording tank offers the dual advantage of slowing thermal fluctuations (which can modulate the EOD) and reducing perturbations that compress the EOD via the insulating walls and air/water surface. Placing the fish in the center of the tank also minimizes field compression from the surfaces.

The magnitude of the surface field compression (at each phase of the EOD) can be readily estimated using the Method of Images (see Sec. 10). An overflow port near the top of the tank maintains a constant water level during steady inflow of respiration water, and provides a convenient route to recirculate the water and keep it fresh.

Supports for the anesthetized or paralyzed fish can perturb the field, and thus should be small and nonconductive. The fish's head was supported by a respiration glass tube, tapered in a flame, cut, and fire polished, so as to fit into the fish's mouth. A small ring of bone wax helped seal the tube rigidly and direct the respiration water to the gills. The respiration tube had a 90° vertical bend ~15 cm from the mouth, bringing it out of the water, and a second horizontal bend ~10 cm further along to connect it to a 3-axis manipulator mounted on the tank wall. Flexible supports for the fish's body and tail were constructed by gluing several cm of insulated solid ~22 ga wire to 1/8" Plexiglas posts. A dab of silicone RTV glue insulated the wire ends (which, if not done, could introduce significant field perturbations by forcing water at the ends to be equipotential). The wires could be readily bent to comply with the curvature of the fish's body and hold the immobilized fish gently but rigidly in any desired orientation. The posts were inserted into a ~8 × 20 × 1/2" Plexiglas plate drilled with numerous 1/8" holes, providing additional degrees of freedom to accommodate various sizes of fish and orientations. This plate sat on the tank bottom and could be easily slid and rotated to the center and align the fish with the coordinate axes defined by the electrode-positioning robot.

Respiration water came from jugs on a shelf ~1.5 m above the tank. Three jugs were plumbed together with stopcocks to switch doses of anesthesia during and after the experiments. The combined output connected to a glass tube lying along the bottom and edge of the recording tank to equalize the temperature of the respiration water. A flexible tube routed the respiration water to the glass mouthpiece, as well as providing an entry through its wall for an insulated wire connected to a #20 gauge silver wire recording electrode at the end of the mouthpiece. Respiration flow rate was regulated with a pinch valve on this flexible tube. Fine adjustment of the pinch valve provided surprisingly sensitive and predictable control of EOD frequency, which helped stabilize the EOD during recording sessions.

A 0.25 × 4 inch graphite rod in the tank corner provided a low impedance ground to reduce common-mode 60 Hz from the recording electrodes. This was connected with a heavy gauge wire to a common ground point for the electronics, a computer, and other devices.

3. ELECTRODES

Electrodes perturb the EOD by introducing current to the tank (due to electrochemistry and amplifier input offset) by their finite impedance to ground

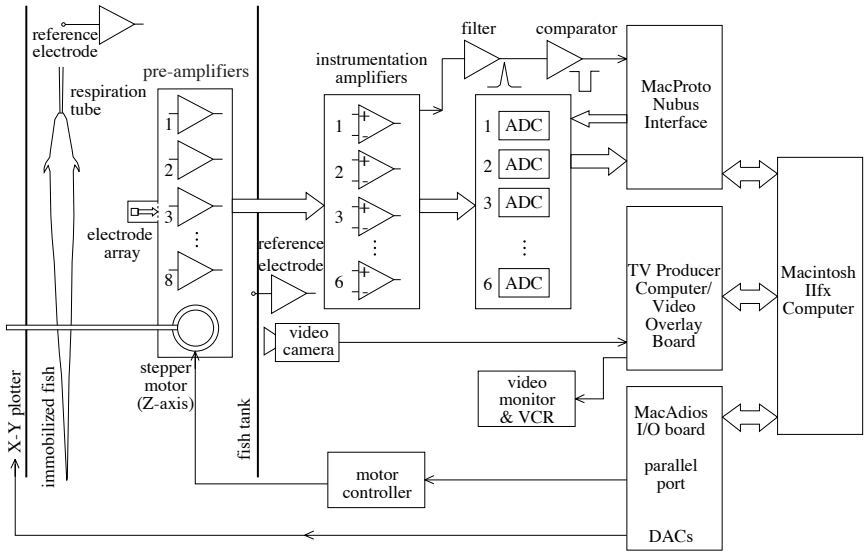

Fig. 21.1: Schematic representation of the EOD field mapping apparatus. (From Rasnow et al., 1993).

through the amplifier (shunting current through an artificial path) and finite size (forcing the water at their surface to be equipotential). Let's examine each of these factors further.

Electrochemistry between a metal electrode and water can be decomposed into frequency domain components: a DC half-cell potential and noise at higher frequencies. Electrophysiologists have long known that Ag/AgCl electrodes have low DC offset and are quiet. Silver also has the advantage of a low melting point. Placing a silver wire in a Bunsen burner flame results in an approximately spherical ball at the end. Letting these electrodes sit in tap water provided adequate AgCl for stable recordings. DC components were never directly measured, and the residual DC was filtered with software.

Amplifier loading of electrodes can be virtually eliminated by directly coupling the electrodes to a high impedance (e.g. JFET) op-amp in a follower configuration (Horowitz and Hill, 1989). Furthermore, keeping the follower close to the electrodes, and placing the unshielded wires in 1 mm OD wickless glass electrophysiology capillaries reduced capacitive loading and noise pickup. Although the amplifier should have a high impedance to ground, the electrode should have low impedance to the water. The electrical model of a small metal electrode in a fresh water fish tank is dominated by spreading resistance given by:

$$R_E = \frac{\phi}{I} = \frac{1}{I}\int E \cdot dl = \frac{1}{I}\int_{r_e}^{\infty} \frac{\rho I}{4\pi r^2} dr = \frac{\rho}{4\pi r_e} \qquad \ldots (1)$$

where ρ = water resistivity and r_e = electrode radius. Typical values of 2 kΩ-cm and 100 μm respectively correspond to an electrode impedance ~20 kΩ and a corresponding thermal (Johnson) noise density of:

$$e_n=(4kTR_E)^{1/2} \sim 18 \text{ nV}/\sqrt{\text{Hz}}, \quad \text{... (2)}$$

where k is Boltzman's constant and T is the absolute temperature. With care, Johnson noise will dominate the total experimental noise (i.e. other noise sources can be controlled below this level). Thus, it is beneficial to minimize spreading resistance by lowering water resistivity and/or increasing electrode radius. Unfortunately, lowering R_E by a factor of two requires a 4-fold change in either ρ or r_e. Also, there are other trade-offs.

Decreasing water resistivity compresses the EOD field, especially near the fish (but in a quantitatively different way than the tank walls do). More EOD current flows and the transdermal potential increases, but the field attenuates more rapidly with distance. Without possible compensatory mechanisms, electric fish would appear further apart to each other in low-resistivity water. Electric images, especially that of dielectric objects, are intimately dependent on water resistivity (Rasnow, 1996). Thus, this parameter should be carefully chosen and controlled.

An electrode of radius r_e perturbs the field proportional to $(r_e/r)^3$ at a distance r. To differentially measure the near field at a resolution ~1 mm, it is not practical to make the electrodes within an array substantially larger than ~200 μm without each electrode affecting the measurements of its neighbors.

Two practical solutions for near-field mapping are flexible arrays that conform to the fish's body, and a rigid 3-dimensional array of electrodes positioned approximately at 4 vertices of a 1 mm cube, permitting differential recordings from which the electric field vector could be derived (Fig. 21.2). For both, the electrode tips are approximately spherical 150–250 μm diameter silver balls, formed by melting a 75 μm diameter silver wire in a Bunsen burner flame. Teflon insulation was stripped before melting, and a thin coat of silicone or epoxy was applied to re-insulate up to the ball end. Prior to melting the electrode, a short length of this wire was delicately soldered to #30 gauge Kynar insulated copper wire-wrap wire and pushed through a 1 mm O.D. glass capillary tube that was tapered in a physiology electrode puller. All support structures (e.g. epoxy) near the electrodes were small and included numerous gaps to minimize field perturbations.

4. POTENTIALS, FIELDS, AND REFERENCES

The electric potential is a differential quantity requiring a local reference somewhere in the fish tank circuit. Two issues should be considered regarding the reference electrode. First, its resistance is a source of Johnson noise and

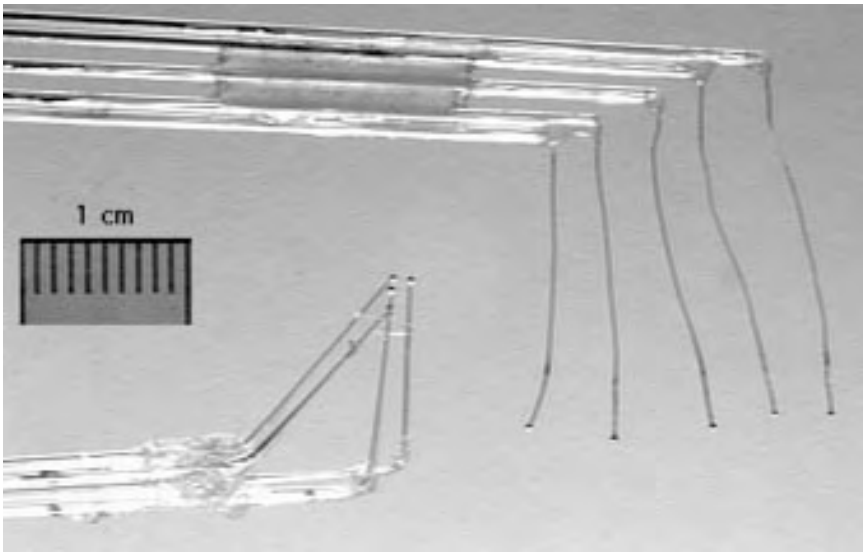

Fig. 21.2: Rigid (top) and flexible (bottom) electrode arrays used for mapping the EOD field and skin potential, respectively. Small holes within the glue, and gaps between the glass tubes reduce the field distortions from the support structures. (From Rasnow et al., 1993).

should thus be minimized. Hence, a larger reference electrode is beneficial, but it can't be too isolated (e.g. at the end of a long tube, where tube resistance may exceed spreading resistance). Second, any potential on the reference electrode (relative to a hypothetical electrode at infinity) will contribute a systematic error. This can be minimized by placing the reference electrode on the wall of a *large* tank near the zero-potential 'plane'. Strange looking potential maps may be the result of a non-zero potential on the reference electrode (relative to infinity). However, computing the electric field (potential gradient) from such data will remove this kind of artifact.

Estimating an electric field component requires four empirical parameters: the simultaneous waveforms at two nearby locations and the position vectors of those exact locations. The relative uncertainty of each of those measurements add (in quadrature) to the relative uncertainty of the electric field component; therefore it is critical to have precise positioning accuracy as well as exact voltmeters. The two waveforms can be measured either relative to a distant reference, and subtracted in software, or the potential subtraction can be done in a differential amplifier before digital conversion. Likewise, a rigid electrode array can have fixed relative positions, or the electrodes can be positioned sequentially with a precision robot. Rigid electrode arrays recorded differentially offer in principle the highest fidelity, since EOD variability and temporal misalignment do not contribute additional error terms. A method to determine relative positions with extreme accuracy is described in Sec. 10.

5. ELECTRODE POSITIONING AND MONITORING SYSTEMS

Although many commercial robot systems are available offering precise automated positioning, integrating a system over a large recording tank may require a degree of customization. Nevertheless, today, one would certainly choose more modern components than the antiquated analog X–Y plotter and custom stepper motor that I used to achieve 13 × 16 × 3 inches of travel of the electrode array and preamplifier. Regardless of choice, the positioning system should be capable of gently and repeatably bringing the electrodes in contact with the fish's skin under electronic control, and rapidly slewing the array around the recording tank. Throughput of measurements away from the fish is likely to be limited by the time required for vibrations of the electrode array to dampen.

During recording sessions, lasting hours, it is likely that the fish may, at some time, move slightly or drastically. Videotaping the experiment through a chroma-keyed computer overlay system solved this problem, enabled using flexible electrode arrays to map potentials on the skin surface, and provided a means to resolve most subsequent data inconsistencies. Chroma-keying is the technology used by television weather forecasters to appear in front of weather maps, and additional applications to experimental neuroscience have been described (Hartmann et al., 2000). A consumer video camera displayed a real-time view of the fish and electrode array in the background of a computer window. The fish's body was traced, and sequential electrode positions were marked by mouse on the computer screen (Fig. 21.3). Resolution was one pixel, which generally corresponded to approximately 500 μm. Even small movements of the fish were readily apparent, as the video image moved out of register with the static body outline. The fish's position was then precisely readjusted and the mapping experiment resumed. Each experiment was recorded on videotape, with the mouth reference EOD on one audio channel and an open microphone for recording comments on the other.

6. ELECTRONICS

Each electrode was connected to a high impedance JFET op-am follower (LF356) mounted nearby on the stepper motor platform. These amplifiers have rated voltage noise density of 12 nV/√Hz and current noise of 0.01 pA/√Hz. Quieter chips are now available, but one should verify performance empirically (see Sec. 9), as specifications may be generated under other conditions. The current noise through the electrode resistance makes a negligible contribution. Thus out of the preamp, the noise density increases just 10% above the Johnson noise:

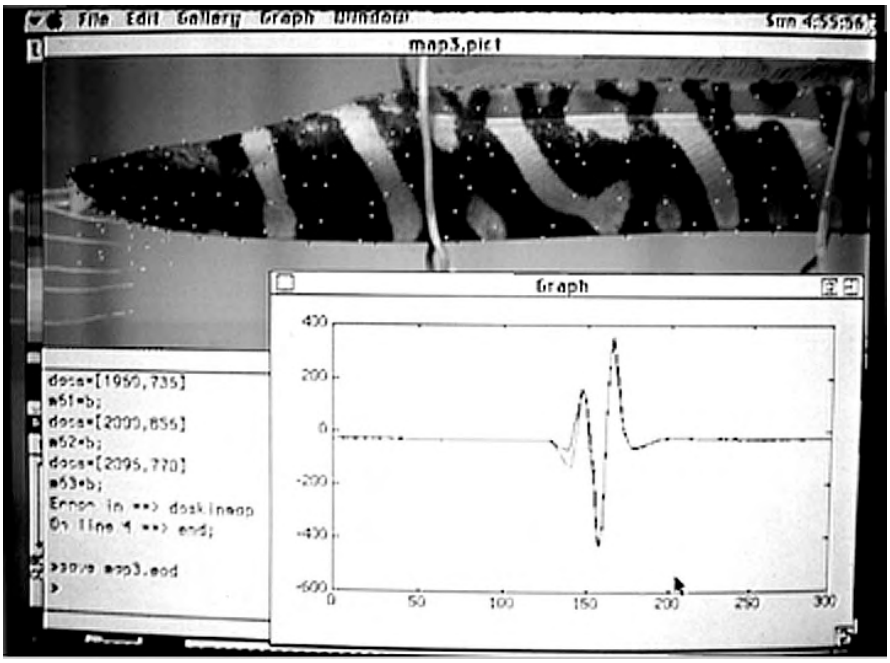

Fig. 21.3: Video-taped frame of a mapping experiment. Chroma-keying was used to superimpose live video of the fish with an outline of its body and recording electrode locations. Images of the waveforms and command window were also recorded on the videotape. (From Rasnow et al., 1997).

$$e_n = \sqrt{(18^2 + 12^2)} = 20 \text{ nV}/\sqrt{\text{Hz}} \quad (3)$$

The follower outputs were routed to instrumentation amplifiers (IA) with jumper-selectable gains of 10, 100, 200, or 500, suitable for near and far field measurements of most wave and pulse EODs. Each follower output could be connected to any (and multiple) IA input. The IA outputs connected to ADC boards (see below). System noise was measured at ~30 nV/√Hz or 3 μV RMS over 10 kHz bandwidth (see Fig. 21.6).

A phase reference signal was generated from the potential difference between two stationary electrodes (usually placed in the mouth and on the tank wall lateral to the fish). This signal passed through a 60 Hz active twin-T notch filter[1] and a 200 Hz bandpass filter tuned to the fish's fundamental frequency, to a comparator with variable DC bias, producing a digital pulse at approximately the same phase of each EOD cycle. The potential before the bandpass filter was also recorded on an ADC channel.

[1] A Hum Bug (http://www.quest-sci.com/pr02.htm) maybe a superior alternative to an active notch filter for removing 60 Hz, but it may introduce artifacts with some EODs.

7. ANALOG-TO-DIGITAL CONVERSION

Without anti-aliasing filters, an ADC folds higher frequency signals into the passband at full amplitude. This means, for example, that a 30 kHz signal (or signal component) sampled with a 50 kHz ADC (25 kHz Nyquist bandwidth) will appear indistinguishable from a 20 kHz signal of the same amplitude. To avoid this error, broadband analog signals must be low-pass filtered before digitization. However, care must also be taken that the anti-aliasing filter doesn't cause significant gain or phase error in the passband. This typically requires complex filter designs and sampling at much higher frequencies than the maximum frequency of interest. ADCs can introduce artifacts other than aliasing, such as sample skew from sequentially switching between inputs, and noise, which often far exceeds one bit for converters housed in electrically noisy computer cases. Fortunately, a few simple tests will reveal many artifacts of the data acquisition system (Fig. 21.4). Of multiple ADC designs, I found a delta-sigma converter highly advantageous, although not without drawbacks: temperature and DC stability can be poor, requiring DC to be subtracted in

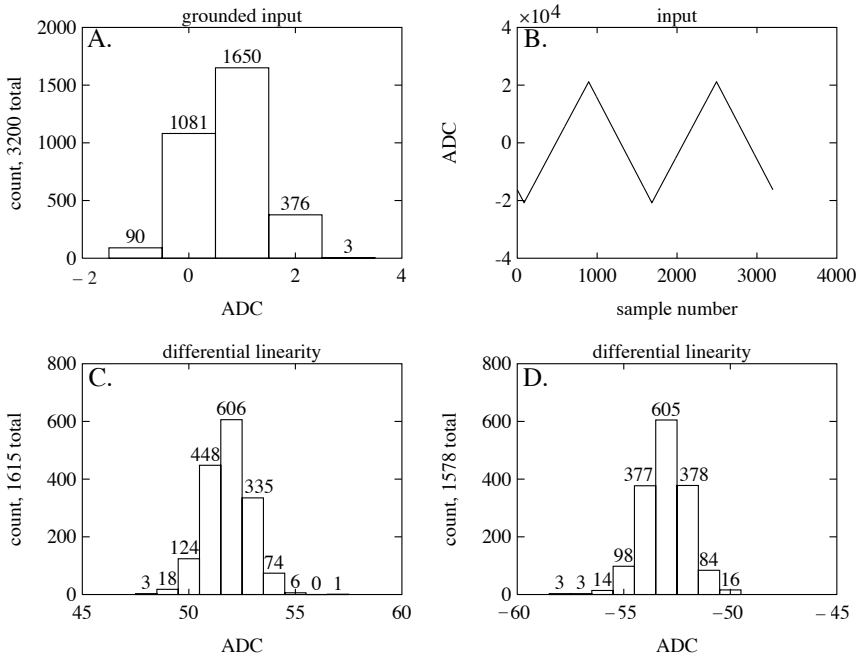

Fig. 21.4. A. With inputs grounded, the ADC outputs are clustered within 4 counts. B. Differential linearity was measured with a slow triangle wave. The difference between successive samples on the positive (C) and negative (D) slope ramps were constant to within 8 counts or 3 bits. (From Rasnow, 1994).

software. Delta-sigma's also have very slow transient responses, and thus cannot be rapidly multiplexed or externally triggered. My solution was to employ separate converters for each IA and multiplex (bus) their tri-state digital outputs. The 6 converters ran continuously and synchronously. The software command to acquire data would first synchronize with a bit transition generated from the phase reference channel before reading a block of samples. Thus, the digitized waveforms had upto 22 μsec of jitter, but better than 1 μsec alignment was commonly achieved with digital signal processing, as described next.

8. DIGITAL FILTERING AND PHASE ALIGNMENT

Wave-type EODs have virtually all of their energy focused in the fundamental and harmonic frequency components. The EOD can be filtered and dramatically compressed by implementing a comb filter in the frequency domain. One note of caution, however, is that the Fourier transform is ill-conditioned and can introduce significant artifacts if there is a discontinuity between the amplitude of the last and first sample of the input. 'Windowing' is one common approach to ensure the endpoints are the same (usually zero), but window functions introduce other artifacts. A simple solution is to trim the length of the time domain waveforms to be an integral number of periods. To minimize any discontinuity caused by residual 60 Hz contamination, an integer number of EOD periods as close as possible to an integer number of periods of 60 Hz (typically 1–3) was used. The continuity of the digital sample was constantly monitored visually, by displaying the last period of the waveform record *followed* by the first period, and the number of samples collected was adjusted as necessary to maintain continuity.

The Fast Fourier Transform (FFT) is actually much *less* efficient at filtering harmonic EOD signals than the Fourier transform. This is because the FFT computes the amplitudes and phases of all frequencies, whereas only just a few harmonic amplitudes and phases are required (typically N~10). Thus, for time domain data of length T (~1600), complex Fourier coefficients are computed in advance ($G = e^{-i\omega nt}$ for $n = 1 \ldots N$, $t = 1 \ldots T$). The matrix multiplication, A = G * data results in N complex amplitudes representing the filtered EOD compressed by ~80:1.

One of the simultaneously recorded channels was always a stationary phase reference. The phase of its fundamental was determined and multiples were subtracted from each of the harmonics to precisely align all sequential measurements. By working in the frequency domain, even if the EOD frequency drifts, a phase error does not accumulate at the end of the EOD; rather, it is distributed among the data.

Pulse EODs are not as amenable to frequency domain processing (and, in fact, the FFT can introduce more ringing artifacts than the noise it removes). Finite Impulse Response (FIR) filtering proved advantageous for filtering pulse EODs, and phase alignment was accomplished by solving for the maxima of the cross correlation of all reference channel waveforms, and interpolating (linear or cubic splines) to the offset of the correlation maxima. Once again, this method was able to achieve much greater EOD alignment precision than the ADC sampling interval, by weighing all the data in the waveforms.

9. FREQUENCY RESPONSE, GAIN CALIBRATION, AND NOISE

The frequency and phase response of the measurement system can be easily verified by measuring waveforms from the electrodes in a water-filled metal can connected to a function generator. An alternative to sweeping the frequency of a sinusoid and taking multiple measurements is to measure a square wave and compare the FFT to its theoretical harmonic components (Fig. 21.5).

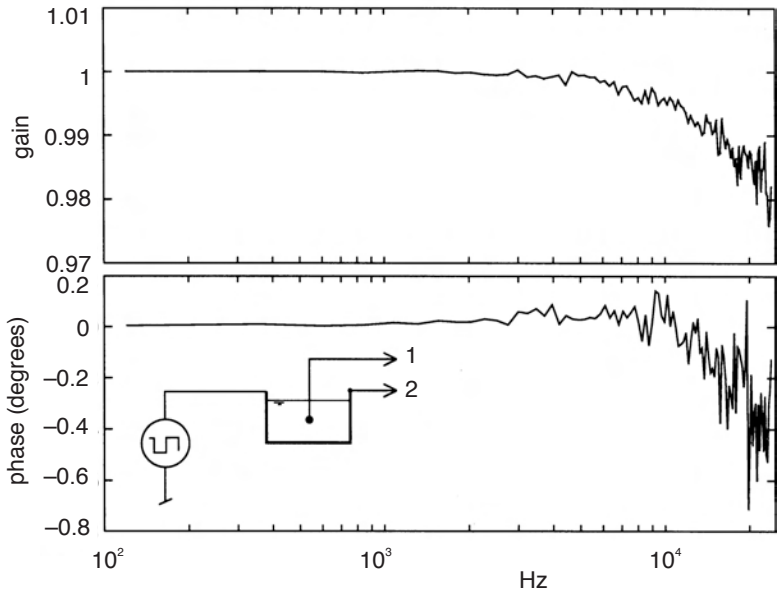

Fig. 21.5: Bode plot (with expanded vertical scale) showing frequency and phase response of the measurement system. The electrode was immersed in water within a metal can, which was connected to a 120 Hz square wave generator (inset). The odd harmonic amplitudes and phase were computed by Fourier analysis and compared to theory. High frequency noise is an artifact from the decreasing amplitude of these square wave components.

Uncorrected channel-to-channel gain differences can lead to huge artifacts in small potential differences. A sine wave is more suitable for precise gain determination for each channel. A voltage divider attenuated the function generator voltage on the can to compensate for the IA gain, yet permitted accurate and precise measurement with a voltmeter (don't forget the √2 ratio between the computed Fourier amplitude and RMS value measured by most voltmeters).

Noise is often measured by estimating the amplitude of the 'hash' or height of the trace on an oscilloscope. This is not only subjective, but can be highly prone to artifacts, especially with digital or high-bandwidth analog oscilloscopes. Avoidable sources can be hiding in the hash of a >20 MHz oscilloscope. The Tektronix 5000 or 7000 series with 7A13 amplifier are ideal oscilloscopes for this analog application. The oscilloscope is critical for verifying that the ADC input contains insignificant energy above its aliasing frequency, but from then on, the best instrument to measure and analyze noise is the EOD data acquisition system. Grounding inputs at different levels of the signal path can isolate noise and artifacts (Fig. 21.6).

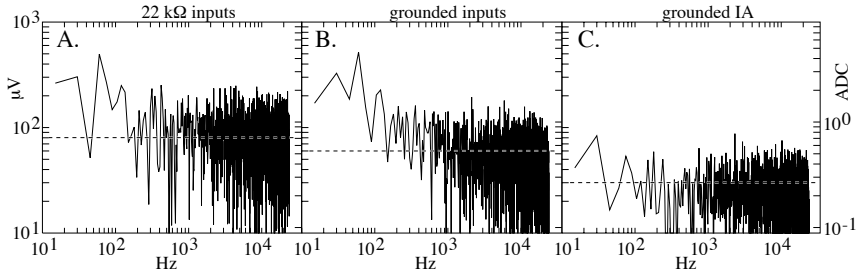

Fig. 21.6: Noise amplitude spectra from a pair of 22 kΩ electrodes (A), grounded preamp inputs (B), and grounded instrumentation amp inputs (C). Each frequency bin has 30 Hz of bandwidth, thus the anticipated noise levels would be 80, 60, and 30 μV per bin (dashed lines). (From Rasnow, 1994).

10. ELECTRODE GEOMETRY CALIBRATION FOR ELECTRIC FIELD ARRAYS

An ideal electrode array for measuring the electric field vector would have spherical electrodes located at precisely (x,y,z) = (0,0,1), (0,1,0), and (1,0,0) relative to an identical reference electrode at the origin. Needless to say, a hand-built array of epoxy and melted glass and silver will deviate from the ideal, and these systematic deviations must be measured and accounted for. The geometry of an electrode array can be determined to incredible precision by mapping a known electric field and optimizing the geometric model to

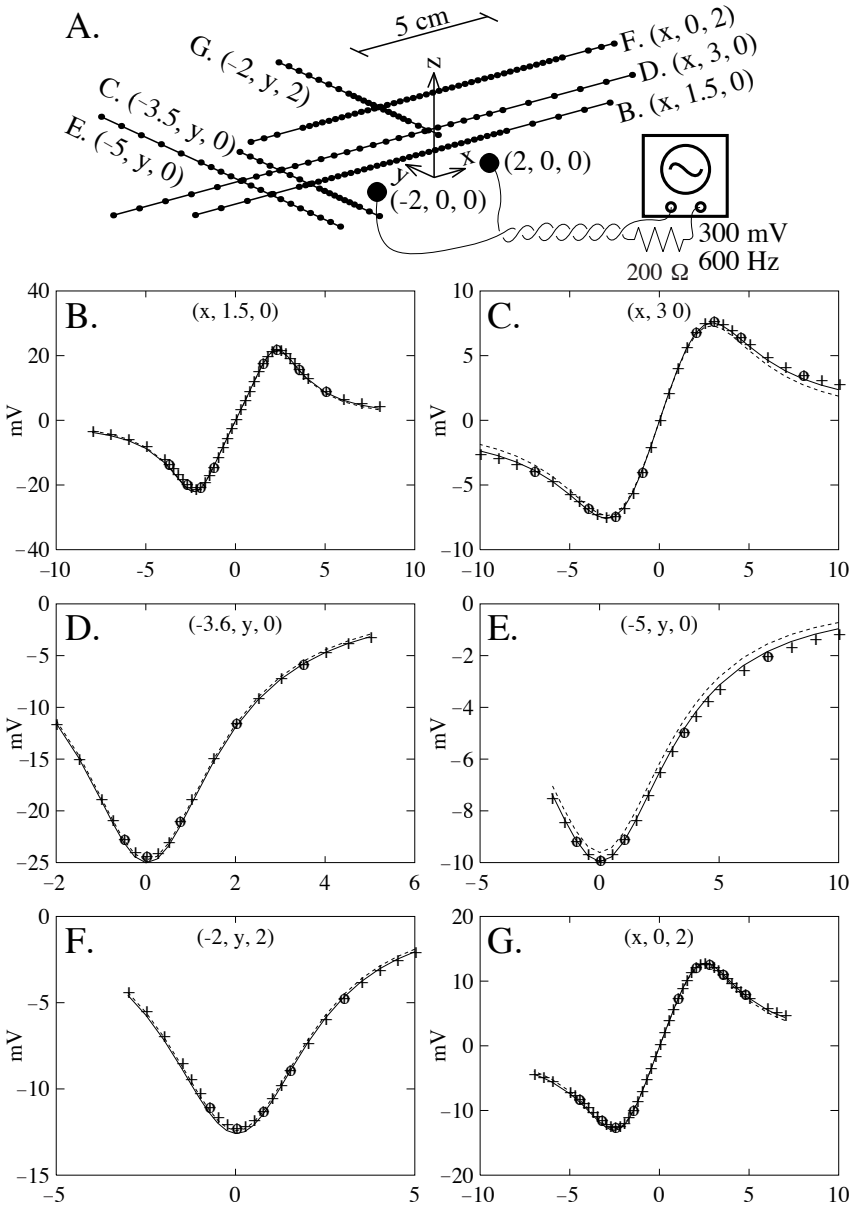

Fig. 21.7: Measured and theoretical potential along six lines (A) around a dipole. Measured values are denoted by '+' and 'o' (only the later were used for the optimization to reduce computation time). Lines are theoretical potentials using the optimized pole coordinates of (x, y, z)/cm = (–2.085, 0.114, –0.114) and (2.202, 0.026, –0.143). The solid line includes image charges for the vertical water surfaces. (From Rasnow and Bower, 1996).

minimize the error between measurements and theory. This was done in the series of steps described next. A dipole was made from two 1/8 inch diameter stainless steel ball bearings soldered (with an acid solder flux) to insulated wire wrap wires held rigid on 1 mm O.D. glass capillaries 4 cm apart. This structure was placed near the center of the recording tank and connected through a 200Ω series resistor to a function generator. With sinusoidal amplitude approximately 300 mV at 600 Hz, the dipole moment is similar to *A. leptorhynchus* in 20kΩ water. In dipole-centered coordinates the poles were at approximately (±2, 0, 0) cm and measurements were made along 6 lines parallel to the x, y, and z axes (Fig. 21.7A). Three IAs and ADC channels measured the differential voltages in the array, a fourth channel measured potential between the array origin and an electrode on the tank wall near the zero-potential plane, and a fifth channel was a stationary phase reference.

Theoretically, a current, **I**, entering a ball bearing (in an infinite tank) will cause a radial current and field,

$$\mathbf{E} = \frac{\rho \boldsymbol{I}}{4\pi r^2}\hat{\mathbf{r}} \qquad \ldots (4)$$

Thus, by superposition, the field from a discrete dipole in an infinite tank, with poles at $\mathbf{x}_1$ and $\mathbf{x}_2$, is:

$$\mathbf{E}(\mathbf{x}) = \frac{\rho \boldsymbol{I}}{4\pi}\left(\frac{\mathbf{x}-\mathbf{x}_1}{|\mathbf{x}-\mathbf{x}_1|^3} - \frac{\mathbf{x}-\mathbf{x}_2}{|\mathbf{x}-\mathbf{x}_2|^3}\right) \qquad \ldots (5)$$

and the potential is:

$$\varphi(\mathbf{x}) = \frac{\rho I}{4\pi}\left(\frac{1}{|\mathbf{x}-\mathbf{x}_1|} - \frac{1}{|\mathbf{x}-\mathbf{x}_2|}\right). \qquad \ldots (6)$$

The finite size of the tank can be accounted for by placing 'image charges' equidistant from the water surfaces. This 'Method of Images' results in a rapidly converging series (only image charges from the shallow vertical surfaces proved significant). Parameters ρ and *I* were measured with conventional meters. The initial visual estimate of the pole locations resulted in considerable error and was refined by optimization: the mean squared error between theory and measurement was minimized using a Nelder-Mead simplex algorithm (Matlab's fminsearch, www.mathworks.com), by adjusting the six coordinate values of the two poles. Results (Fig. 21.7) show tight fit with plausible corrections of <2 mm.

If the array is in a uniform field $\mathbf{E} = (E_x, E_y, E_z)$, then the measured potential differences between electrodes are proportional to the field and the interelectrode distances:

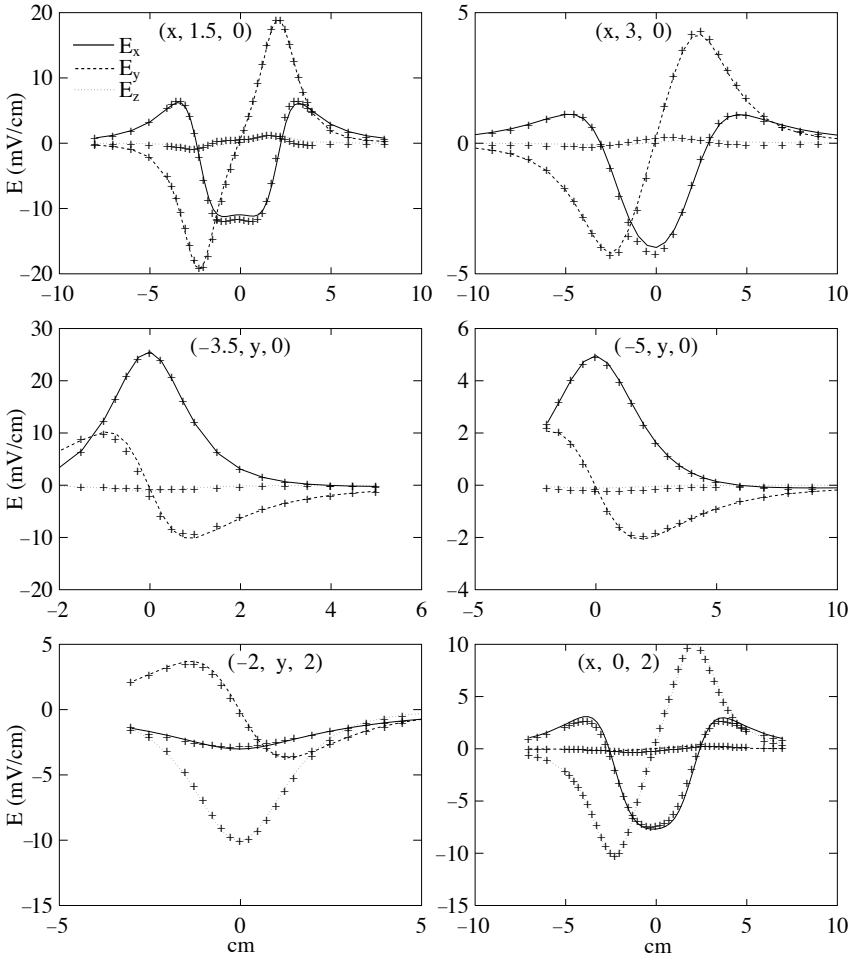

Fig. 21.8: The theoretical field components (curves) were computed from measurements of the water conductivity, function generator current, and pole locations. The measured field components ('+') were computed using differential potential measurements from the electrode array and the optimized array geometry (Eqns. 7 and 8). Measurements were made along the paths in Fig. 21.7A. (From Rasnow and Bower, 1996).

$$\begin{bmatrix} \varphi_2 - \varphi_1 \\ \varphi_3 - \varphi_1 \\ \varphi_4 - \varphi_1 \end{bmatrix} = \begin{bmatrix} x_2 - x_1 & y_2 - y_1 & z_2 - z_1 \\ x_3 - x_1 & y_3 - y_1 & z_3 - z_1 \\ x_4 - x_1 & y_4 - y_1 & z_4 - z_1 \end{bmatrix} \begin{bmatrix} E_x \\ E_y \\ E_z \end{bmatrix} \quad \ldots (7)$$

where electrode k at position (x_k, y_k, z_k) is at potential φ_k. The electric field components were computed from the potential differences by mathematically

inverting this equation. The interelectrode distance matrix and its inverse were estimated using a second optimization, this time minimizing the difference between the field components computed in this manner, and the theoretical field of a discrete dipole (Eqn. 5). Since the field decays faster than the potential, the vertical water surfaces had smaller effects, and were ignored. Multiple dipole mappings of an array resulted in interelectrode distances and standard deviations of:

$$\Delta x / \text{mm} = \begin{bmatrix} 2.203 \pm 0.014 & 0.264 \pm 0.003 & 0.177 \pm 0.022 \\ 0.452 \pm 0.006 & 1.315 \pm 0.000 & -0.038 \pm 0.002 \\ 0.290 \pm 0.015 & 0.053 \pm 0.068 & -1.231 \pm 0.034 \end{bmatrix} \quad \ldots (8)$$

The average standard deviation of 18 μm is far less than could probably be achieved by visual or other methods. The high accuracy of this method is demonstrated in Fig. 21.8.

As a final consistency check of the array calibration, differential field components computed using the interelectrode distance matrix were compared with the numerical gradient of the potential measured relative to a distant reference, with an electric fish as the source (Fig. 21.9). Only the fundamental amplitude and phase are shown, but agreement between the two methods is similar for the other harmonics.

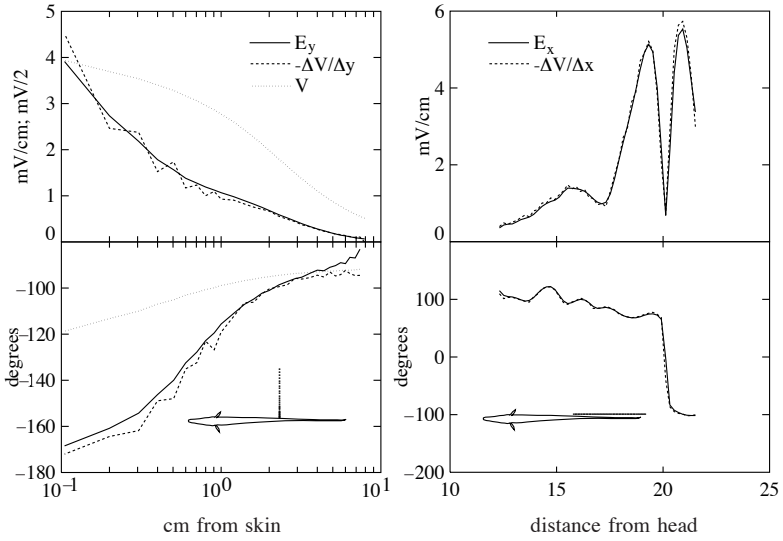

Fig. 21.9: A. Amplitude and phase of the fundamental frequency electric field component, computed from the interelectrode distance matrix (solid line), and the numerical derivative of the potential (dashed line). The potential is also shown (dotted line). B. Same as A, along the tail 6 mm lateral of the fish's centerline. (From Rasnow, 1994).

11. MAPPING A FISH

Apteronotids with neurogenic EOs were immobilized with intramuscular injection of 30–50 μg Flaxedil (gallamine triethiodide). Other types of fish were tranquilized with 3 ppm etomidate hydrochloride in a holding tank and subsequently administered in the respiration water. Significant care was taken to align the fish's body axes with the robot and electrode coordinate system, using a high contrast grid behind the recording tank as reference, viewed through the chroma-keyed video. Midplane maps were usually done with the fish upside down so the ventral fin protruded above the supports. Dorsal and ventral maps were made in the same half-plane of the tank but with the fish precisely rotated 90 or 270° from the midplane map.

12. SPATIAL INTERPOLATION AND VISUALIZATION OF WAVEFORMS

Measurements were made at variable density, highest near the EO and skin where the field and its rate of change are greatest (Fig. 21.10). A Delaunay

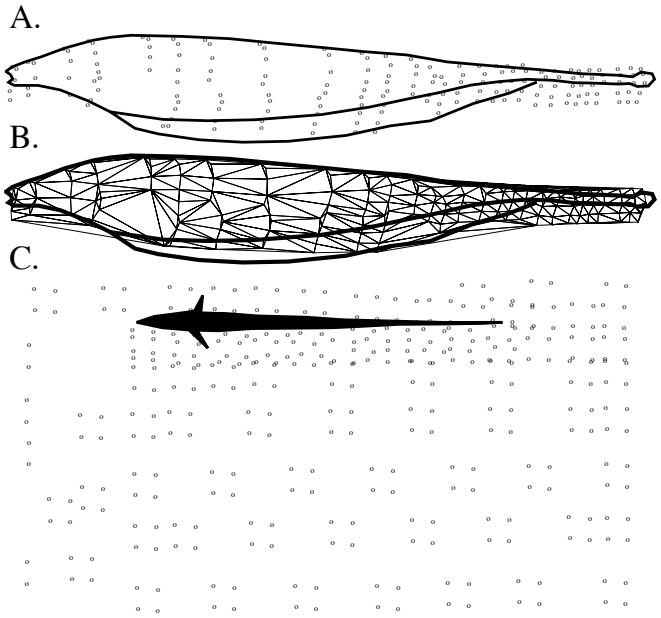

Fig. 21.10: A. The fish's profile with measurement positions from a five-electrode flexible array. B. Triangular elements corresponding to the measurement points for interpolating potential maps. C. Measurement positions for a midplane potential map using a 4-electrode square array. (From Rasnow et al., 1993).

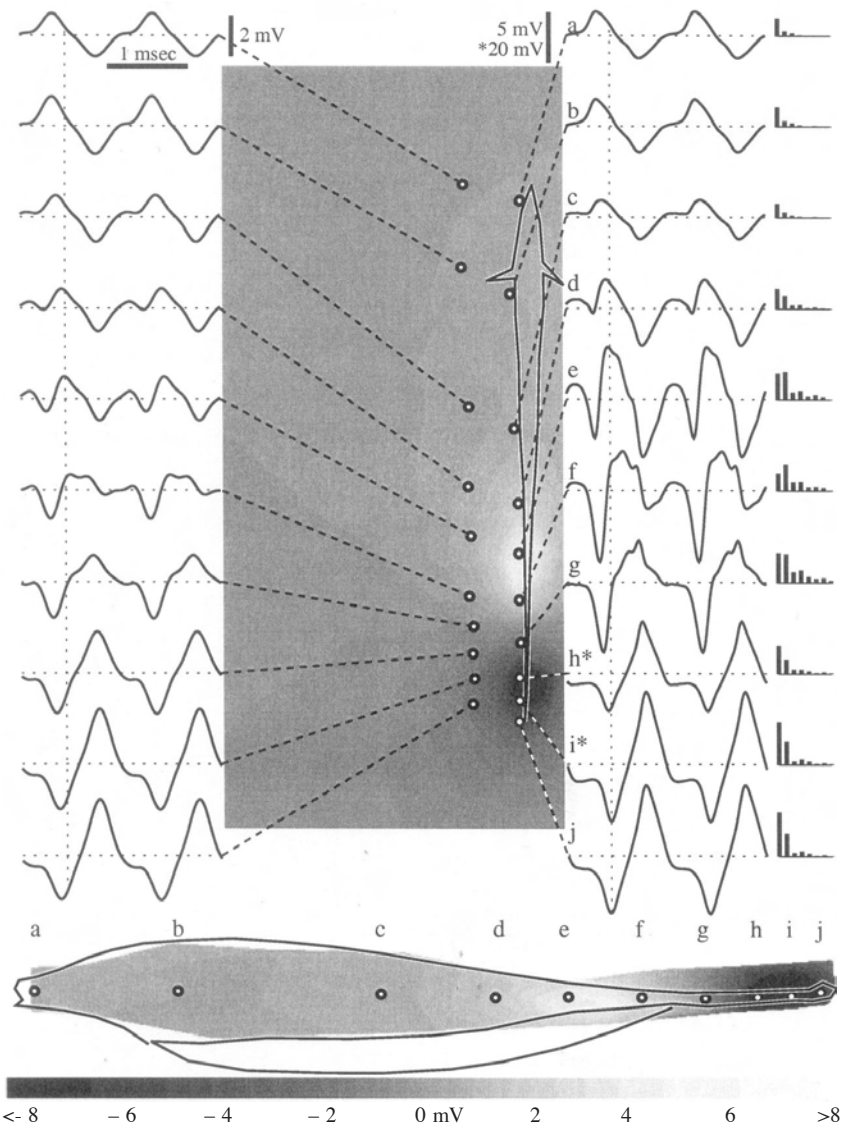

Fig. 21.11: Illustration of how the EOD waveforms measured at different locations were used to construct pseudocolor images. The waveforms shown (two EOD periods) were measured at points indicated by the black circles. The beginning of each waveform is in phase with the positive slope zero crossing of the EOD recorded in the fish's mouth. On the right side are amplitude spectra of the fundamental and the next seven harmonics, with the same vertical scale as the corresponding waveforms. The grayscale images correspond to the phase marked on the waveforms by the vertical dotted lines. The letters above the skin view indicate the corresponding locations of the waveforms measured on the fish's midline. (From Rasnow et al., 1993).

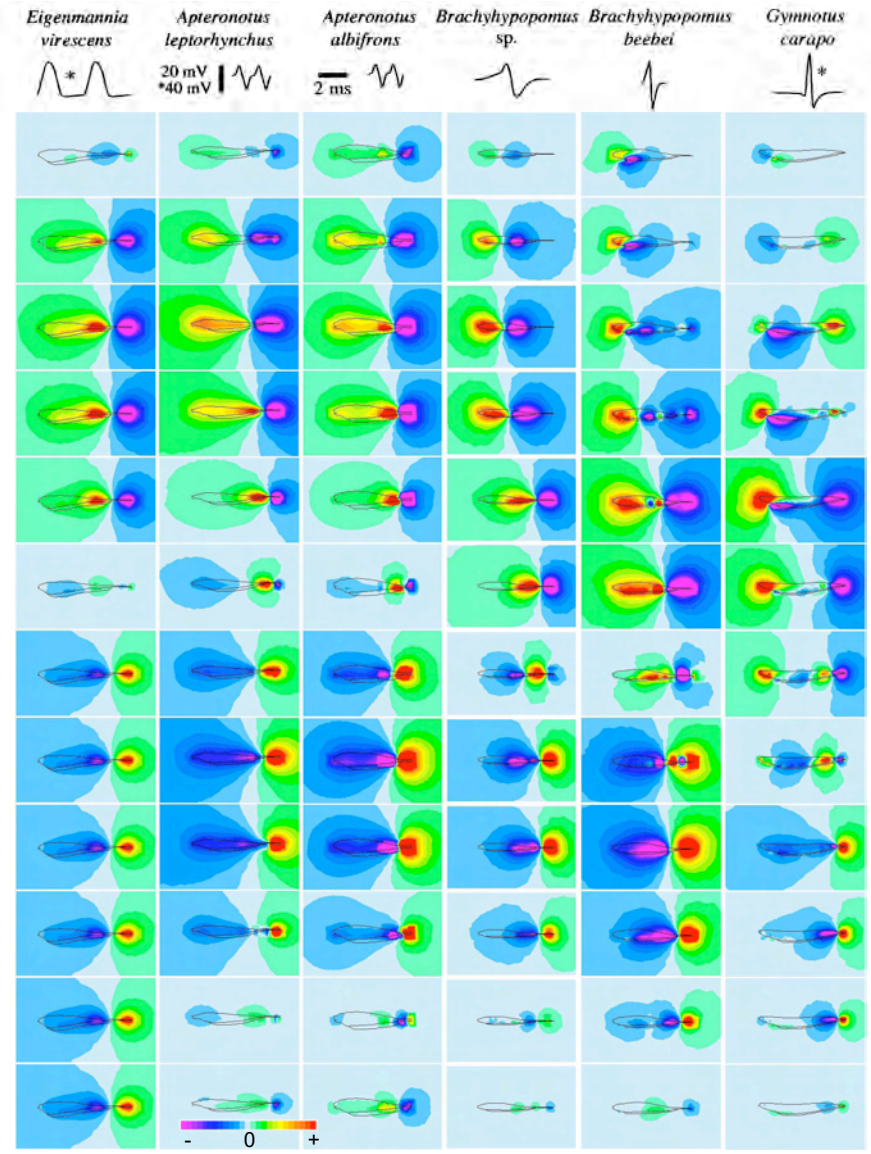

Fig. 21.12: EOD potential maps of 6 electric fish species, rendered in pseudocolor at 12 successive phases. (From Assad et al., 1999).

tessellation was used to interpolate between the measurements, in part because it facilitated comparisons with finite and boundary element simulations using an identical grid (Assad, 1997). Each phase of the temporally aligned potentials and computed field components were linearly interpolated at each pixel of

the triangular elements. The resulting value was rendered as grayscale or pseudocolor images (Figs. 21.11, 21.13), and successive images from each phase were assembled into montages and animations (Fig. 21.12 and www.alumni.caltech.edu/~rasnow).

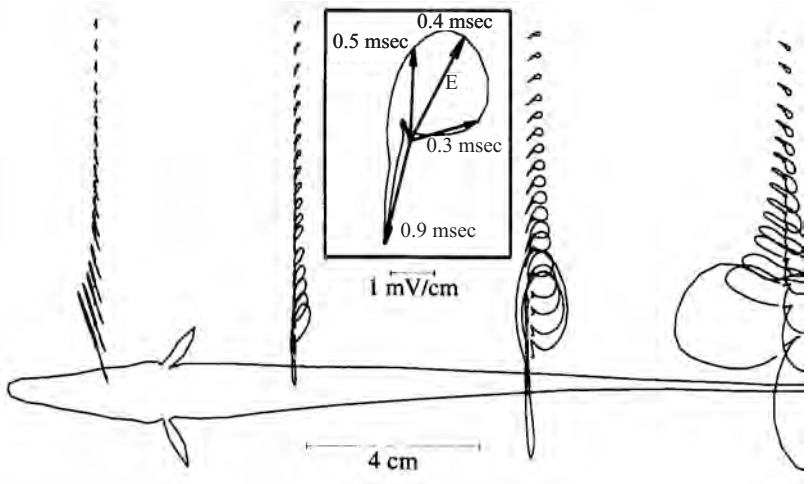

Fig. 21.13: The electric field vector along four lateral lines in the midplane of *Apteronotus leptorhynchus*. The initial field vector is drawn from each measurement point (dots) and the tip of the vector is traced at subsequent phases. Inset shows four example phases of the field vector. The field vectors rotate counterclockwise in the caudal part of the body, whereas rostral of the gill, only the magnitudes and sign, but not the direction, changes during the EOD cycle. (From Rasnow and Bower, 1997).

13. DIMENSIONAL REDUCTION: AMPLITUDE, PHASE, VECTOR DIAGRAMS

As complex as the above description is for measuring the EOD potential and field, interpreting and understanding these complicated, multidimensional functions of space and time is even more challenging. The potential and field were decomposed into frequency, amplitude, phase, and perturbation components, each accentuating different aspects of the electrosensory experience. For example, a polar plot of the field vector (Fig. 21.13) shows how the direction of the electric field and current change during the EOD. However, this 2-dimensional representation can be misleading when the 3 orthogonal field component are significant, which may occur for closely interacting fish or where the EO is asynchronous and far from the midline (e.g. Fig. 21.14). Sometimes even a simple change in coordinates or reference can have profound effect on one's ability to understand the data. For example,

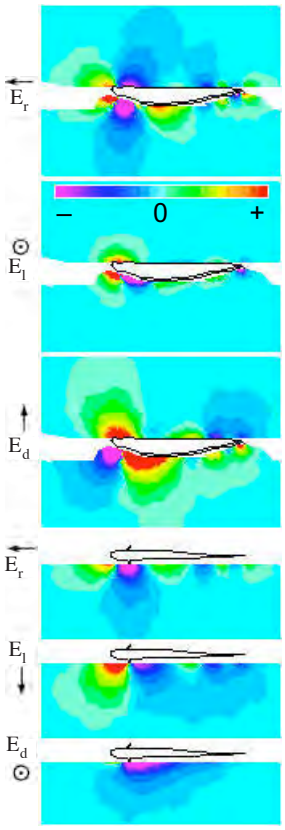

Fig. 21.14: The electric field of *Gymnotus carapo* at the 4th phase displayed in Fig. 21.12, approaching the positive peak of the head-to-tail waveform. Separate pseudocolor maps indicate the instantaneous magnitudes of the rostral, lateral, and dorsal components (E_r, E_l, E_d) in the dorsoventral plane (top 3 images) and midplane (lower 3). The current circulates near the fish, flowing from the mouth at the top of the body towards the base of the ventral fin. Multiple sources and sinks are active along the EO. These multipoles attenuate rapidly with distance, however, the non-radial circulating current is measurable beyond half a body length in the midplane (bottom). (From Assad et al., 1999).

whereas it is natural experimentally to measure distance between the fish's skin and the proximal surface of an object, including the object's radius in the distance measure makes the relative width of the corresponding electric image linearly dependent on object distance. This provided a key clue towards hypotheses about how objects are perceived electrically (Rasnow, 1996; Rasnow and Bower, 1997).

14. SIMULATIONS

Numerical simulation is another powerful method for studying EODs and their perturbations, and tends to be highly complementary to field mapping. In particular, simulations of weak fields are most accurate, whereas noise dominates the corresponding measurements. Conversely, measurements of strong fields near the fish are most accurate but simulations here are prone to errors due to high spatial and temporal frequency components and strong gradients. In the domain of overlap, each method can be useful in validating the other. Figure 21.15 shows how careful electric image measurements and simulations can closely agree over a range of parameters. These measurements were done with a flexible array on the fish's skin, and the simulations used a semi-analytical model of the object and unperturbed EOD measurements

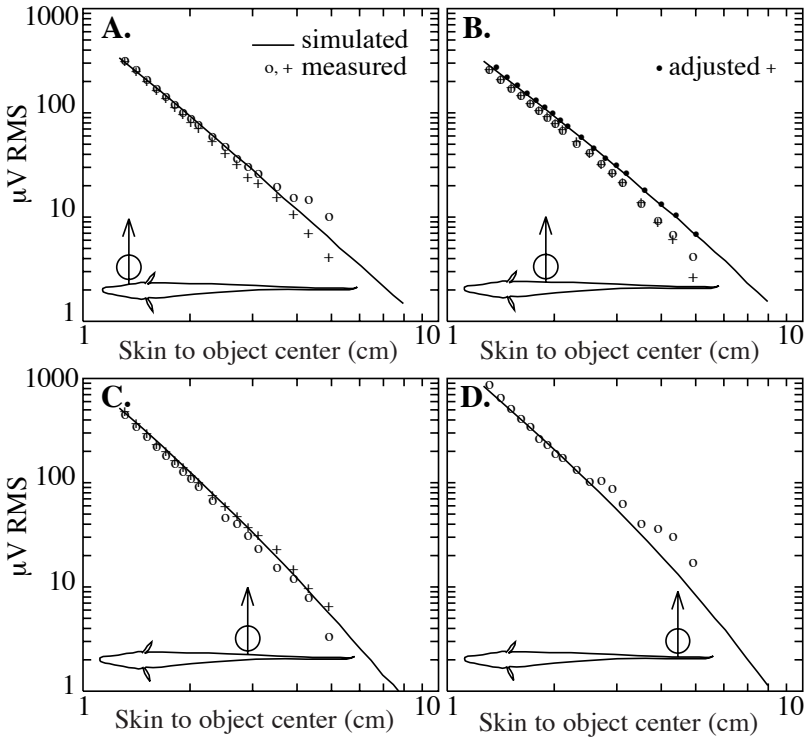

Fig. 21.15: Simulated and measured electric image amplitudes generally agree over more than two orders of magnitude. The measurements were repeated twice in A–C. In B, discrepancy between simulations and measurements were virtually eliminated (dots) by two minor corrections: adding 0.5 mm to the fish-object distances, and adding 4 μV to the measured 1.85 mV EOD amplitude with the object at infinity (a 0.2% correction). (From Rasnow, 1996).

(Rasnow, 1996). This approach was employed and extended to model electric images of *Daphnia* to the fish's detection limit (Nelson et al., 2002; Nelson, 2005). Simulations are likely to become more common and useful in understanding electric sense as computing power increases and software becomes more accessible.

15. CONCLUDING REMARKS

EOD mapping as described here has brought us a long way towards understanding the electroreceptive periphery. However, discovering natural bases for studying sensory information processing is a most challenging endeavor. In more commonly studied modalities such as olfaction and vision, rigorous debate continues over how odors and visual stimuli are represented and decomposed in neural computations. Clearly, Cartesian electric field components are not a natural electrosensory basis, but they do form a complete representation of the electrosensory information outside the fish's body and on the sensory array, from which any number of projections or decompositions can be made. Thus, field mapping as described here is a logical stage for further study of electric sense.

Biologists and especially electrophysiologists are often accustomed to recording bioelectric signals of extremely low amplitude (e.g. the gating motion of a single ion channel protein). Nevertheless, measuring much stronger EOD signals poses new challenges. The electrode physics as described here are different, and electric fish are sensitive to less than part-per-thousand perturbations superimposed on large bias signals. Exploring these electric perturbations requires care and accuracy, and trade-offs between effort, equipment, subjects, and protocols. The theory presented here will hopefully guide experimenters on how to make compromises most appropriate for their particular questions and circumstances.

Although my work has focused on understanding electrolocation of electrically passive objects, a similar approach can be applied to the study of electric communication. Here the 'object' is another fish that actively generates an electric field. The active source significantly extends the range of electrocommunication and adds other forms of complexity. The electric image has additional spectral components resulting in sum and difference frequencies or beats. The other fish is a distributed source, and only at large separations will be accurately modeled as a dipole. As electric fish approach each other, their body's impedance will induce passive electric images, and even closer, the two fish may change the loading on each other's EO, and induce EOD modulation behaviors like chirping and jamming avoidance that profoundly change the EOD and the electrosensory environment. We can only begin to wonder what the qualia of such an encounter must be for an electric fish.

REFERENCES

Assad, C. 1997. *Electric Field Maps and Boundary Element Simulations of Electrolocation in Weakly Electric Fish*. Ph.D. thesis, California Institute of Technology, Pasadena, CA. University Microfilms Inc. Ann Arbor MI.

Assad, C., B. Rasnow and P.K. Stoddard. 1999. Electric organ discharges and electric images during electrolocation. *J. Exper. Biol*. 202: 1185–1193.

Dennett, D.C. 1988. Quining qualia. In: *Consciousness in Contemporary Science*. A. Marcel and E. Bisiach (eds). Oxford University Press, Oxford.

Hartmann, M., C. Assad, B. Rasnow and J.M. Bower. 2000. Applications of video mixing and digital overlay to neuroethology. *Methods* 21: 385–391.

Horowitz, P. and W. Hill. 1989. *The Art of Electronics*, 2nd Edition, Cambridge University Press, Cambridge.

Nelson, M.E. 2005. Target detection, image analysis and modeling In: *Electroreception* (Springer Handbook of Auditory Research) T.H. Bullock, C.D. Hopkins, A.N Popper, R.R. Fay (eds). Springer-Verlag, New York.

Nelson, M.E., M.A. MacIver and S. Coombs. 2002. Modeling electrosensory and mechanosensory images during the predatory behavior of weakly electric fish. *Brain Behav. Evol*. 59: 199–210.

Rasnow, B. 1994. *The Electric Field of a Weakly Electric Fish*. Ph.D. Thesis, California Institute of Technology. University Microfilms.

Rasnow, B. 1996. The effects of simple objects on the electric field of *Apteronotus*. *J. Comp. Physiol.* A 178: 397–411.

Rasnow, B. and J.M. Bower. 1996.The electric organ discharges of the gymnotiform fishes I. *Apteronotus leptorhynchus. J. Comp. Physiol*. A 178: 383–396.

Rasnow, B. and J.M. Bower. 1997. Imaging with Electricity: How Weakly Electric Fish Might Perceive Objects. In: *Computational Neuroscience: Trends in Research*. J.M. Bower (ed.). Plenum, New York, pp. 795–800.

Rasnow B., C. Assad and J.M. Bower. 1993. Phase and amplitude maps of the electric organ discharge (EOD) of *Apteronotus leptorhynchus*. *J. Comp. Physiol*. A 173: 751 –752.